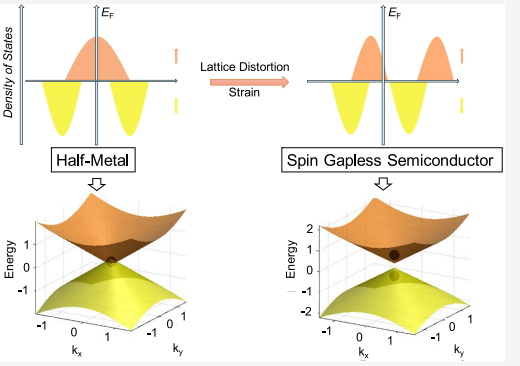
JACS
JOURNAL OF THE AMERICAN CHEMICAL SOCIETY
pubs.acs.org/JACS
Article

Emergent Ferromagnetism and Spin Gapless Conductivity in Atomically Thin $Co_3Sn_2S_2$ Nanosheets

Abhinav Pancholi,[#] Pranav Negi,[#] Kartik Samanta, Abhishek Das, Premakumar Yanda, Shishir Kumar Pandey, and Subhajit Roychowdhury*

Cite This: https://doi.org/10.1021/jacs.5c08223
Read Online
ACCESS | Metrics & More | Article Recommendations | Supporting Information

ABSTRACT: Spin-gapless semiconductors (SGSs) represent an intriguing class of quantum materials that bridge the gap between half-metallic ferromagnets and conventional semiconductors, offering promising avenues for spintronic applications. The discovery of intrinsic ferromagnetism in ultrathin two-dimensional van der Waals crystals has further fueled interest in exploring magnetism at the ultimate two-dimensional limit. Here, we demonstrate the growth of environmentally stable, atomically thin $Co_3Sn_2S_2$ nanosheets via a simple hydrothermal method. These nanosheets exhibit robust ferromagnetism with a Curie temperature of ∼100 K and remarkably, host a spin-gapless semiconducting (SGS) state, distinct from the well-known half-metallic Weyl ferromagnetism observed in the bulk counterpart. Structural analysis reveals that enhanced lattice distortion and strain effects in the nanosheets, induced by reduced dimensionality and surface defects, play a critical role in stabilizing this phase. Williamson-Hall analysis confirms the presence of strain, while DFT calculations reveal that strain-induced lattice distortions annihilate the Weyl points and the emergence of SGS semiconductivity. Charge transport measurements indicate a Mott variable-range hopping mechanism, while temperature-dependent conductivity suggests a coexistence of semiconducting and weakly gapless features. These findings not only establish atomically thin $Co_3Sn_2S_2$ nanosheets as a novel platform for SGS physics but also open up exciting possibilities for strain-engineered topological phases and next-generation spintronic and quantum technologies.



INTRODUCTION

Semiconductors and semimetals bridge the gap between insulators and metals, yet their interconnection remains surprisingly underexplored. While semiconductors drive modern electronics and semimetals have shaped quantum physics for decades, understanding their crossover could unlock new advancements in materials science and technology.[1−5] After the discovery of graphene in 2004, van der Waals (vdW) layered materials have been widely studied for their fundamental properties and technological potential.[6−9] Recently, ferromagnetic two-dimensional (2D) materials have garnered significant attention for their unique properties arising from low dimensionality and electronic constraints. The emergence of 2D vdW ferromagnets—including CrI_3, $Cr_2Ge_2Te_6$, $CrSe_2$ and Fe_3GeTe_2—has opened new frontiers in magnetic phenomena at the extreme 2D limit, paving the way for spintronic and information storage applications.[10−13] However, their low Curie temperature (T_c) and spin polarization hinder practical spintronic applications, making it imperative to develop 2D ferromagnets with enhanced T_c and spin polarization through theoretical and experimental efforts. Despite their promising properties, most 2D vdW ferromagnets studied so far suffer from poor stability under ambient conditions. Their instability complicates direct synthesis, as atomically thin monolayers are highly sensitive to synthetic and postsynthetic processing conditions. Therefore, achieving scalable synthesis of air-stable 2D magnets is crucial for advancing this field and enabling practical applications.

Among various 2D ferromagnetic materials, 2D spin-gapless semiconductors (SGSs) stand out as promising candidates for high-efficiency spintronic devices.[14−16] First proposed by Wang in 2008 in Co-doped $PbPdO_2$, SGSs serve as a bridge between magnetic semiconductors and half-metals.[15] These materials exhibit a unique band structure: a semiconducting bandgap for the minority spin channel and a zero bandgap for the majority spin channel at the Fermi level.[17,18]

Recently, several Heusler compounds such as CoFeCrGa, CoFeCrAl, and CrVTiAl have been identified to exhibit spin-gapless semiconductor (SGS) characteristics.[18−20] These systems are particularly interesting because their electronic

Received: May 15, 2025
Revised: September 4, 2025
Accepted: September 15, 2025

Downloaded via UNIV SCIENCE AND TECHNOLOGY CHINA on September 23, 2025 at 04:54:42 (UTC).
See https://pubs.acs.org/sharingguidelines for options on how to legitimately share published articles.

ACS Publications
© XXXX American Chemical Society

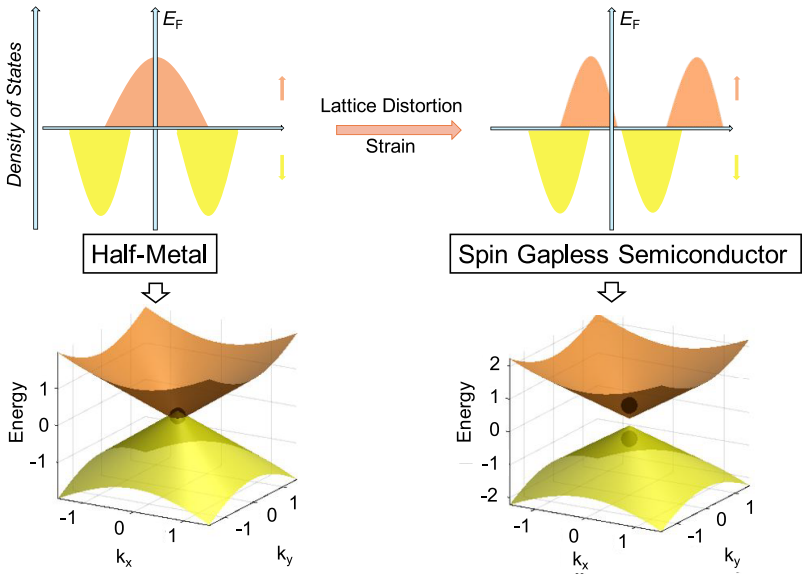


Figure 1. Schematic illustration of band opening from Weyl semimetal to spin-gapless semiconductor.

structure is highly sensitive to lattice imperfections, antisite disorder, and atomic site occupancy, yet they continue to manifest SGS-like behavior under such conditions. Experimental studies have shown that the spin-gapless behavior persists even in the presence of disorder in the system mentioned above.[18−20]

In a disordered spin-gapless system, disorder leads to broadening of the electronic states near the Fermi level, thereby generating mixed spin-polarized transport and subtle deviations from the ideal semiconducting response. To understand this, Kharel et al. proposed a two-carrier model for conductivity in spin-gapless and disordered spin-gapless semiconductors.[19] According to this model, one spin channel in a disordered-SGS exhibits a small band overlap, while the other retains a finite semiconducting band gap. This dual-channel conduction accounts for the nearly linear resistivity behavior with temperature and the observed negative temperature coefficient of resistivity in these materials.

SGSs offer several advantages, including minimal energy requirements for electron excitation from the valence to the conduction band and the simultaneous full spin polarization of both electrons and holes. Their unique band structure allows for the generation of spin-polarized currents from both charge carriers and the ability to switch between n-type and p-type spin-polarized currents under an external field.[17,18] These characteristics make SGSs highly attractive for next-generation spintronic applications, paving the way for energy-efficient magnetic devices.

To achieve a ferromagnetic spin-gapless semimetallic phase, a natural starting point is a half-metallic Weyl ferromagnet, where the controlled annihilation of Weyl points can open a gap in one spin channel. To validate this concept, we focus on $Co_3Sn_2S_2$, a well-established half-metallic ferromagnet that hosts magnetic Weyl Fermions.[21,22]

$Co_3Sn_2S_2$ crystallizes in a quasi-2D crystal structure, featuring alternating hexagonal planes of Sn and S, with a Co_3Sn Kagome layer sandwiched between the S atoms.[23] This unique arrangement gives rise to Weyl points near the Fermi level (E_F), which remain largely free from interference by trivial bands. As a result, the material exhibits a pronounced anomalous Hall effect and a large anomalous Hall angle.[21] Furthermore, its quasi-2D crystal structure, combined with a simple semimetallic band topology, makes it an ideal candidate for exploring novel quantum states. Moreover, the bulk $Co_3Sn_2S_2$ single crystal exhibits a Curie temperature of 177 K.[21]

In recent years, significant efforts have been directed toward synthesizing 2D crystals of $Co_3Sn_2S_2$ using techniques such as focused ion beam (FIB) milling and molecular beam epitaxy (MBE).[24,25] While these methods enable precise control over material growth, they are often limited by stringent processing conditions, making them less feasible for large-scale production of high-quality 2D materials.

To advance the field, it is crucial to develop a more accessible and scalable synthesis approach that ensures high throughput, cost-effectiveness, and ease of material transfer. Moreover, compatibility with established semiconductor fabrication technologies is essential for integrating these materials into practical applications. Establishing such a facile and efficient method for synthesizing the 2D magnetic semiconducting state of $Co_3Sn_2S_2$ would be a significant step toward realizing its full potential in next-generation quantum and spintronic devices. To the best of our knowledge, there are no reports in the literature on the stabilization of a semiconducting phase of $Co_3Sn_2S_2$.

Here for the first time, we demonstrate the emergence of spin-gapless semiconductivity in atomically thin $Co_3Sn_2S_2$ nanosheets (Figure 1). These nanosheets were synthesized using a simple hydrothermal method,[26] enabling the formation of ultrathin layers with well-defined structural characteristics. Magnetic measurements reveal a saturation magnetic moment of approximately 1.5 μ_B per formula unit (0.50 μ_B/Co), confirming that the $Co_3Sn_2S_2$ nanosheets retain robust ferromagnetism at low temperatures. Electrical resistivity measurements further establish a transition to semiconducting behavior, in stark contrast to the bulk $Co_3Sn_2S_2$, which is known as a topological Weyl semimetal. This shift in electronic properties is attributed to enhanced lattice distortion and strain effects induced by the reduced dimensionality and surface defects in the nanosheets, as validated by Williamson-Hall analysis. Our density functional theory (DFT) calculations provide strong theoretical support for this observation,

https://doi.org/10.1021/jacs.5c08223
J. Am. Chem. Soc. XXXX, XXX, XXX−XXX

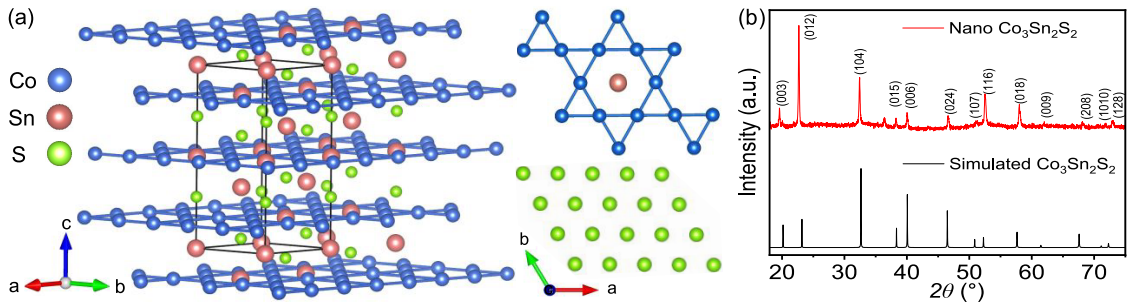


Figure 2. (a) Crystal Structure of $Co_3Sn_2S_2$. (b) Powder X-ray diffraction pattern of as-synthesized $Co_3Sn_2S_2$ nanosheets.

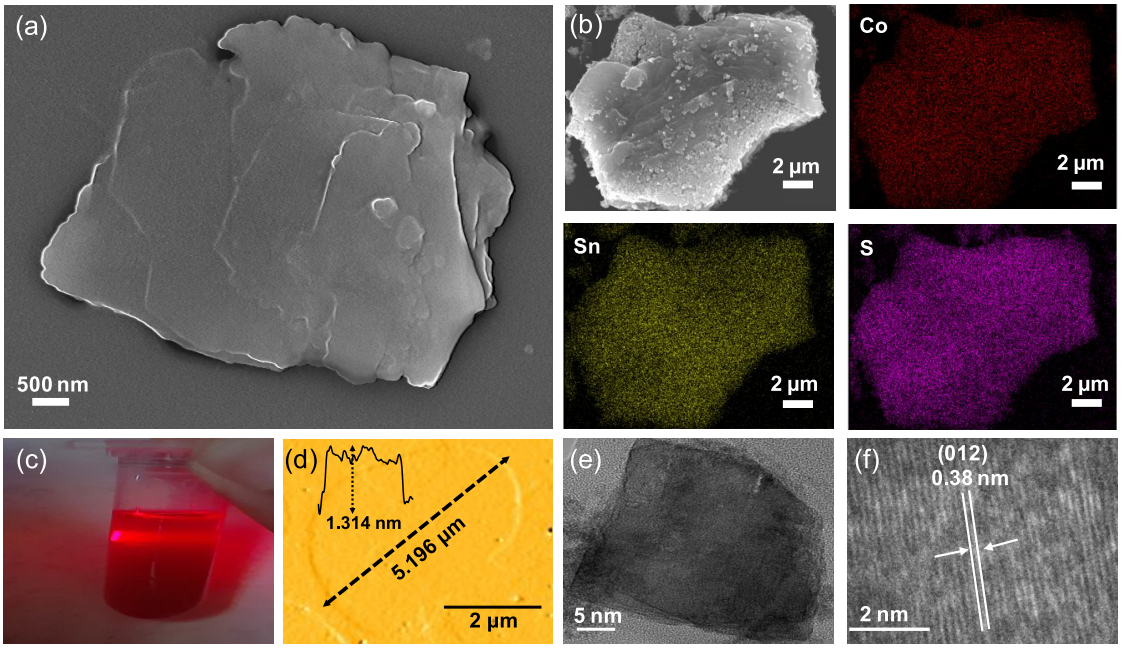


Figure 3. (a) FESEM image and (b) elemental color mapping for $Co_3Sn_2S_2$ nanosheets. (c) Tyndall light scattering effect of the nanosheets dispersed in isopropanol solution. (d) AFM image of $Co_3Sn_2S_2$ nanosheets. (e) TEM image of $Co_3Sn_2S_2$ nanosheets. (f) HRTEM image of a $Co_3Sn_2S_2$ nanosheet.

revealing that the strain-induced lattice distortions annihilate the Weyl points in the nanosheets, thereby stabilizing the semiconducting state.

RESULTS AND DISCUSSION

The compound $Co_3Sn_2S_2$, part of the Shandite family, crystallizes in a rhombohedral structure (space group $R\bar{3}m$).[23] It consists of $CoSn_4S_2$ octahedral units arranged in a hexagonal close-packed sequence along the *c*-axis. Each Co atom is coordinated by four Sn and two S atoms, forming a distorted octahedron. The Co and S atoms occupy the Wyckoff positions 9e and 6c, respectively. The $CoSn_4S_2$ octahedra connect via face-sharing in the *ab*-plane and corner-sharing along the *c*-axis. The Co atoms form a Kagome lattice through corner-sharing triangles within the Co−Sn layers. There are two distinct Sn sites: Sn(2) at Wyckoff position 3a, centered in Kagome hexagons, and Sn(1) at position 3b, linking adjacent Co−Sn(2) layers. S atoms are positioned above and below the Co−Sn(2) layers, completing the structure (Figure 2a).

We have used a simple two-step hydrothermal method to prepare $Co_3Sn_2S_2$ nanosheets (Table S1).[26] In a typical synthesis, we prepare a solution by dissolving $SnCl_4{\cdot}5H_2O$ in ethanol and $CoCl_2{\cdot}6H_2O$ in distilled water at room temperature. Then, NaOH solution was added to the solution very slowly while stirring the solution continuously. After the dropwise addition, the solution was stirred for 1 h, during which it transitioned from dark purple to pink. The resulting pink precipitate ($Co_3Sn_2(OH)_6$) was purified by washing with water and ethanol, followed by centrifugation at 4000 rpm. In the next step, $Co_3Sn_2(OH)_6$, thioacetamide (acts as a source of sulfur) in ethanol solution was heated at 140 °C for 12 h in a Teflon-lined autoclave. Black powders of $Co_3Sn_2S_2$ nanosheets were purified by washing with water and ethanol (Experimental Section and Figure S1, Supporting Information, SI).

The powder X-ray diffraction (PXRD) patterns of the as-prepared sample can be indexed to pure rhombohedral $Co_3Sn_2S_2$ ($R\bar{3}m$ space group, JCPDS no. 01−084−7267) with lattice parameters of a = 5.4225 Å and c = 12.9890 Å (Figure 2b and Table S3). The elemental composition of the nanosheets sample, as determined by energy-dispersive X-ray spectroscopy (EDAX), closely matches the nominal stoichiometry (Table S2). This consistency confirms that the current synthetic method allows for precise control over the composition, ensuring the successful formation of the desired phase.

https://doi.org/10.1021/jacs.5c08223
J. Am. Chem. Soc. XXXX, XXX, XXX−XXX

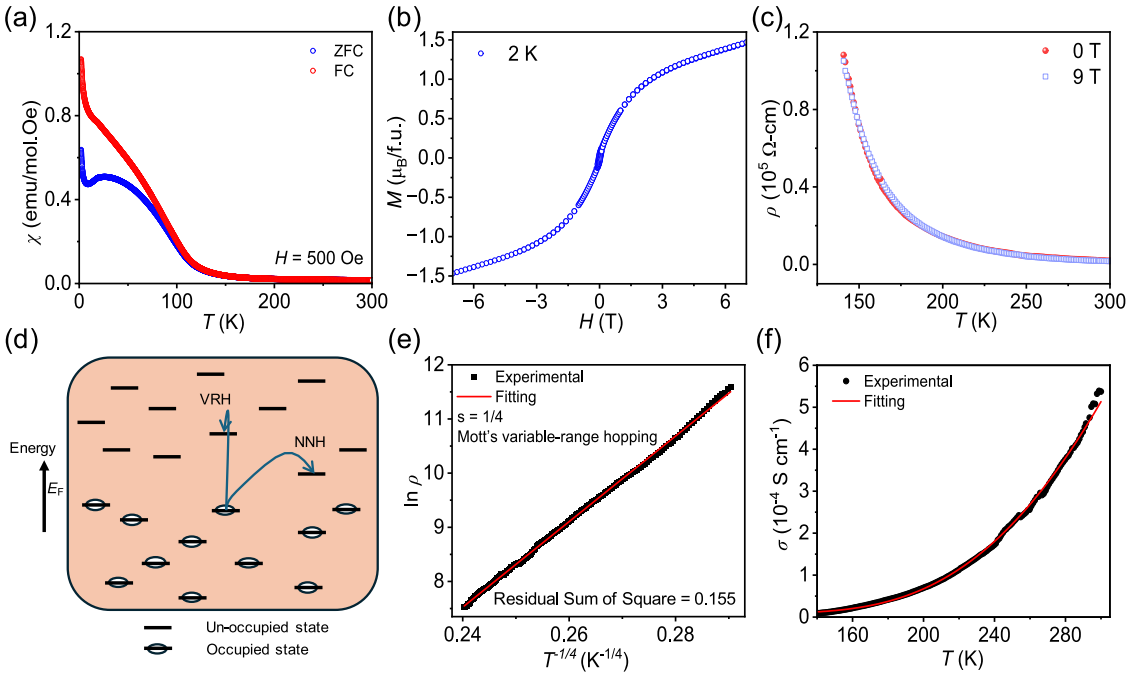


Figure 4. (a) Temperature dependence of ZFC and FC magnetization of nanosheets. (b) Isothermal magnetization curve at 2 K. (c) Temperature dependence of resistivity of $Co_3Sn_2S_2$ nanosheets at 0 and 9 T. (d) Schematic Diagram for hopping-transition mechanism. (e) Resistivity of $Co_3Sn_2S_2$ nanosheets fitted with eq 1 with $s = 1/4$. (f) Zero-field longitudinal conductivity versus temperature fitted with eq 2 (shown by the solid red line).

The surface morphology of the as-synthesized $Co_3Sn_2S_2$ nanosheets was systematically characterized using field-emission scanning electron microscopy (FESEM), atomic force microscopy (AFM), and transmission electron microscopy (TEM). FESEM images reveal the characteristic two-dimensional (2D) morphology of the nanosheets (Figures 3a and S2, SI). Elemental mapping performed during scanning electron microscopy (SEM) confirms the homogeneous distribution of cobalt, tin, and sulfur throughout the nanosheets (Figure 3b and Table S2, SI), attesting to the compositional uniformity of the sample. The colloidal nature of the nanosheets was visually confirmed by the Tyndall light scattering effect observed in a dispersion of $Co_3Sn_2S_2$ nanosheets in isopropanol (Figure 3c).

AFM analysis further validated the ultrathin nature of the nanosheets. As shown in Figure 3d, the height profile obtained from a representative AFM image reveals a thickness of approximately 1.3 nm, which corresponds closely to one unit layer of $Co_3Sn_2S_2$. The lateral dimensions of the nanosheets is ~5.19 μm, highlighting their large aspect ratio and 2D morphology.

TEM provided additional evidence of the nanosheet structure (Figure 3e). High-resolution TEM (HRTEM) images distinctly show lattice fringes with a spacing of 0.38 nm, corresponding to the (012) crystallographic plane of $Co_3Sn_2S_2$ (Figure 3f), further confirming the crystalline nature and phase purity of the synthesized nanosheets.

To investigate the magnetic and electrical properties of the $Co_3Sn_2S_2$ nanosheets, we conducted comprehensive magnetic and electrical transport measurements. The magnetic susceptibility of the nanosheets was measured using both zero-field-cooled (ZFC) and field-cooled (FC) measurements under an applied magnetic field of 500 Oe (Figure 4a). Upon cooling, the $Co_3Sn_2S_2$ nanosheets exhibit a clear paramagnetic to ferromagnetic (FM) transition around 100 K (Figure S3a, SI), which is slightly lower than the transition temperature typically observed in bulk $Co_3Sn_2S_2$.[21] This shift in magnetic ordering temperature highlights the influence of reduced dimensionality on the magnetic behavior of the nanosheets. A similar trend was observed earlier in several other 2D magnetic systems upon dimensional reduction from bulk to nanosheets (Table S4).[27−30]

The isothermal magnetization of $Co_3Sn_2S_2$ nanosheets, measured at 2 K, is presented in Figure 4b. The $M-H$ curve at this temperature clearly confirms ferromagnetic behavior, exhibiting a coercivity (H_c) of ~394 Oe and a saturation magnetization (M_s) of ~1.5 μ_B/f. u. These values indicate that the $Co_3Sn_2S_2$ nanosheets retain robust ferromagnetism at low temperatures, further confirming the preservation of magnetic ordering even in the reduced dimensional form.

Figure 4c illustrates the semiconducting behavior of $Co_3Sn_2S_2$ nanosheets, as evidenced by the increase in resistivity with decreasing temperature over the range of 140 to 300 K under zero magnetic field. This trend reflects a negative temperature coefficient of resistivity ($d\rho/dT < 0$), indicative of the nonmetallic nature of the nanosheets (Figure S3b, SI). Such semiconducting behavior is characteristic of several spin-gapless semiconductor (SGS) materials, including CrVTiAl, CoFeMnSi, CFCG, and Mn_2CoAl,[20,31−33] suggesting that reduced dimensionality may play a role in tuning the electronic transport properties of $Co_3Sn_2S_2$ toward a SGS-like regime.

Carrier transport in semiconductors is primarily governed by the electron hopping mechanism, which typically occurs via two dominant processes: nearest-neighbor hopping (NNH) and Mott's variable-range hopping (VRH).[34,35] These mechanisms differ in how charge carriers move through the disordered system and are distinguished by their characteristic temperature dependence. Figure 4d schematically illustrates the fundamental differences between NNH and VRH transport processes.[35] Mathematically, the two mechanisms can be

https://doi.org/10.1021/jacs.5c08223
J. Am. Chem. Soc. XXXX, XXX, XXX−XXX

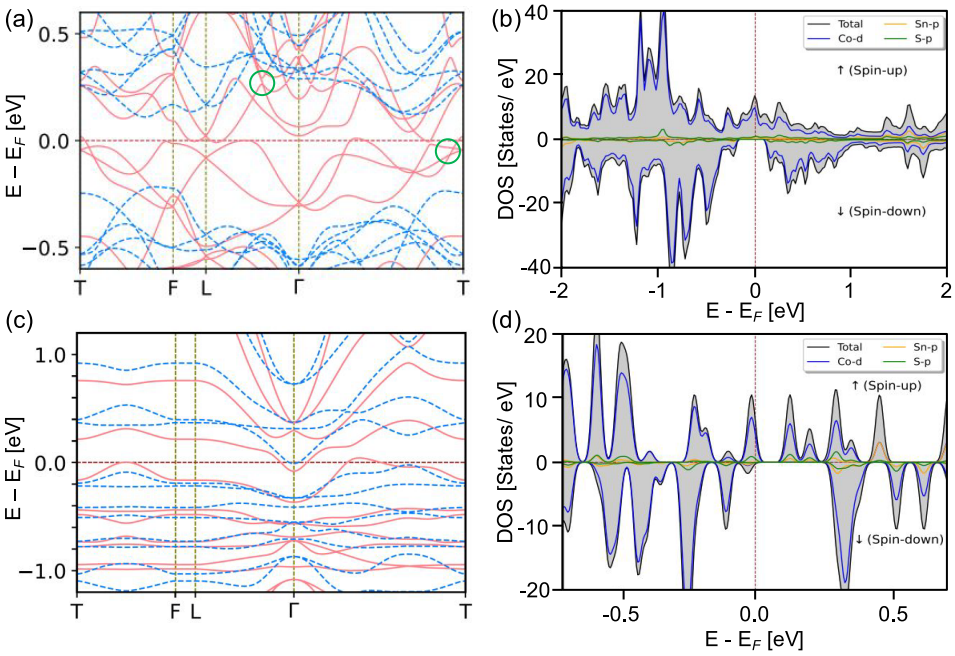


Figure 5. (a) Spin polarized electronic band structure of bulk $Co_3Sn_2S_2$ without SOC. (b) Density of states (DOS) of $Co_3Sn_2S_2$ bulk. (c) The spin polarized electronic band structure of a monolayer of $Co_3Sn_2S_2$ with 10% strain without SOC and corresponding (d) DOS. Red solid line and blue dotted line represents Spin up and Spin down channel, respectively.

differentiated by the exponent s in the exponential temperature dependence of resistivity[35,36]

$$\rho(T) = \rho_0 \exp\left[\left(\frac{T_0}{T}\right)^s\right] \tag{1}$$

Where

$$T_0 = \frac{24}{\pi k_B g(\mu) a^3}$$

In the given expression, the prefactor ρ_0 is determined by the properties of the material. The parameters $g(\mu)$, a and k_B represent the density of states at the Fermi level, the localization states near the Fermi level and the Boltzmann constant, respectively.[35] The exponent s is a constant associated with the electron density near the Fermi level and serves as a diagnostic parameter for identifying the dominant hopping mechanism in a material. Specifically, $s = 1$ corresponds to nearest-neighbor hopping (NNH), while $s = 1/4$ is characteristic of Mott's variable-range hopping (VRH) in three-dimensional systems.[34,35] To determine the nature of charge transport in $Co_3Sn_2S_2$ nanosheets, the longitudinal resistivity data were fitted using eq 1 with $s = 1$ and $s = 1/4$. The quality of the fits was assessed via the residual sum of squares, revealing that the fit with $s = 1/4$ (Figure 4e) provided a significantly better match to the experimental data compared to fits using $s = 1$ or $s = 1/2$ (Figure S4, SI). This finding marks a notable deviation from the metallic-like behavior typically observed in the topological Weyl semimetal state of bulk $Co_3Sn_2S_2$ and strongly indicates that charge transport in the nanosheets is governed by Mott's variable-range hopping mechanism. In the VRH model, the localization length (a) arises from the exponential decay of electronic wave functions in disordered systems. Unlike extended Bloch states, disorder gives rise to localized states near the Fermi level (E_F), where the probability density of an electron decreases as $\psi(r) \propto r^{-n} \exp(-r/a)$.[37] Physically, "$a$" represents the spatial extent of a localized state: a smaller "a" indicates strong localization with electrons confined to atomic scales, whereas a larger "a" implies weaker localization, enabling easier tunneling between sites. Together with the density of states (DOS) at E_F, "a" determines the characteristic hopping temperature, T_0, and thereby controls the temperature dependence of electrical conductivity.

The temperature-dependent conductivity curve (Figure 4f) exhibits a clear exponential behavior, indicative of the presence of a semiconducting gap in the $Co_3Sn_2S_2$ nanosheets. By modeling the temperature dependence of conductivity, $\sigma(T)$, valuable insights can be gained into the carrier activation energies associated with the band gap, offering a deeper understanding of the electronic structure of the material. Such analysis helps distinguish whether the system is gapped, gapless, or metallic, and sheds light on the nature of the band structure near the Fermi level.[20] This approach is crucial for revealing how reduced dimensionality modifies the electronic states and transport behavior in these two-dimensional nanosheets.

To model the temperature-dependent conductivity of $Co_3Sn_2S_2$ nanosheets, we employed the two-carrier model proposed by Kharel et al.[19] This model is particularly suited for disordered spin-gapless semiconductors (SGSs), where one spin channel exhibits a band overlap (gapless), while the other spin channel features a semiconducting band gap. According to this model, the conductivity of the disordered SGS is expressed as a combination of the conductivity through the overlapped channel (σ_{SGS}) and the conductivity through the semiconducting channel (σ_{SC}).[18]

$$\sigma(T) = \frac{1}{\rho(T)} = \sigma_{SGS} + \sigma_{SC} = \sigma_0\left[1 + 2\ln(2)\frac{k_B T}{g}\right] + \sigma_{SC0} e^{(-\Delta E/k_B T)} \tag{2}$$

https://doi.org/10.1021/jacs.5c08223
J. Am. Chem. Soc. XXXX, XXX, XXX−XXX

where σ_0 is the zero-temperature conductivity, g denotes the overlap between the bands in the gapless channel, and k_B is the Boltzmann constant, σ_{SC0} is zero-temperature contribution of conductivity to the semiconducting component, and ΔE gives carrier activation energy.

The solid line in Figure 4f represents the fit using this model, yielding an activation energy (ΔE) of 112 meV, consistent with semiconducting behavior. Furthermore, the fit indicates a small band overlap in the gapless channel, with g ~45 meV, highlighting the presence of a narrow overlap between bands in the otherwise gapless spin channel. The parameter g quantifies band overlap and thus reflects the degree of disorder, providing a measure for how far the system deviates from the ideal SGS state. The observed g value is consistent with values reported for disordered spin-gapless semiconductors (Table S5).[18−20] These results confirm the coexistence of semiconducting and weakly gapless features in the electronic structure of the nanosheets.[18,20]

To investigate the electronic structure of $Co_3Sn_2S_2$ nanosheets, we performed first-principles density functional theory (DFT) calculations for both bulk and thin-film configurations (Figures 5 and S5−S7 and Tables S6−15, SI).

Figure 5a presents the calculated electronic structures of bulk $Co_3Sn_2S_2$. In the absence of SOC, the spin-down channel exhibits a gap of ~0.35 eV, while the spin-up channel remains semimetallic, as also confirmed by the corresponding density of states (DOS) (Figure 5b). Notably, the bands near the Fermi level are predominantly derived from the Co 3d orbitals, with a calculated magnetic moment of approximately 0.33 μ_B per Co atom. This half-metallic character is consistent with earlier reports.[21,38] Moreover, in the spin-up channel, symmetry protected band crossings (nodal line) are observed near the Fermi level along the Γ-L and Γ-T path. Upon including SOC, the nodal ring is gapped out (Figure S5a) and splits into Weyl nodes, in agreement with previous studies.[21,38]

For the monolayer system, we have considered the effect of tensile strain in our DFT calculations which is in well agreement with the experimental results (Tables S3, S6−S9). We have carried out systematic calculations on the monolayer under varying strain conditions (0−10%) (Figure S6). Figure 5c further shows the band structures under 10% tensile strain, without SOC. Interestingly, we find that all band crossings are destroyed even in the absence of SOC, indicating that the nodal ring does not exist in the monolayer limit. Consequently, with SOC included, no Weyl points are expected in the strained monolayer $Co_3Sn_2S_2$ system (Figure S5b). DFT calculated saturated magnetic moment (0.40 μ_B/Co) for monolayer with 10% tensile starin is in agreement with the experimentally observed saturated magnetic moment (0.50 μ_B/Co) (Figure 4b and Tables S10−S15). The enhancement may arise from point defects, disorder, or vacancies inherent to the nanosheet structure, which could also account for the observed differences between the experimental magnetic and transport properties and the idealized DFT results. In order to clarify the origin of the enhanced magnetic moment observed in the strained monolayer, we have carefully examined the effect of strain while keeping the surface termination fixed in all calculations (Tables S10−S15). Our DFT results indicate that the increase in magnetic moment is not solely a surface-related effect. Specifically, when a 10% tensile strain is applied even to the bulk system (without surface terminations), we observe a clear increase in the Co magnetic moment compared to the unstrained bulk (Tables S10−S11). This suggests that the modification of the local electronic structure under strain plays the dominant role in driving the enhancement of magnetic moments.

Moreover, we have carried out DFT calculations for different smearing methods such as Gaussian smearing (0), Fermi smearing (−1), Tetrahedron method (−4), Tetrahedron method with Fermi−Dirac smearing (−14) and Tetrahedron method with Blöch corrections with Fermi−Dirac smearing (−15) for monolayer $Co_3Sn_2S_2$ with 10% tensile strain and observed broadly similar behavior near Fermi level (Figure S7).

In contrast to the bulk material, which exhibits half-metallic behavior, the strained nanosheet displays a transition to a disordered spin-gapless semiconductor phase. This is consistent with our $\rho(T)$ measurements, which suggest SGS characteristics with a slight band overlap in the spin-up channel, as described by a two-carrier transport model for disordered SGS system.[19]

Overall, our calculations clearly demonstrate that reducing bulk $Co_3Sn_2S_2$ to nanosheet form leads to a significant transformation in its electronic properties-from half-metallic to semiconducting-thereby positioning $Co_3Sn_2S_2$ nanosheets as promising candidates for future spintronic device applications.

To understand the origin of the stabilization of SGS phase in $Co_3Sn_2S_2$ nanosheets, we employed the Williamson−Hall (WH) analysis to evaluate the microstrain (ε) present in the samples. The WH approach is based on the following equation[39]

$$\beta \cos\theta = \frac{k\lambda}{D} + 4\varepsilon \sin\theta \tag{3}$$

where β is full width at half-maximum (FWHM), k = 0.9 is the shape constant, λ is the wavelength of Cu−$K_{\alpha 1}$ radiation, D denotes crystallite size, θ is Bragg angle, and ε is the microstrain within the crystal lattice. The Williamson−Hall plots for both nanosheets and bulk samples are presented in Figure S8, SI. From these plots, the slope of the linear fit yields the value of microstrain. The analysis reveals that the bulk $Co_3Sn_2S_2$ sample exhibits significantly lower microstrain, indicative of minimal lattice distortion and a highly ordered crystal structure. In contrast, the nanosheet sample demonstrates a markedly higher microstrain, reflecting substantial lattice distortion and strain. This increased microstrain in the nanosheets arises from reduced dimensionality, enhanced surface to volume ratio, and surface defects, which are inherent to the nanostructured form.

The significant strain present in the synthesized $Co_3Sn_2S_2$ nanosheets leads to the annihilation of the Weyl points, resulting in the opening of a gap in the electronic structure. This transition is further supported by our DFT calculations, which confirm the emergence and stabilization of a spin gapless semiconductor phase in the nanosheets. These findings highlight the critical role of strain engineering in tailoring the electronic and topological properties of quantum materials, offering new avenues for their application in spintronic devices.

CONCLUSIONS

In conclusion, we have successfully stabilized spin-gapless semiconductivity in atomically thin $Co_3Sn_2S_2$ nanosheets. This marks a striking contrast to the bulk semimetallic state, where the emergence of the semiconducting phase is attributed to enhanced lattice distortions and strain effects induced by reduced dimensionality and surface defects. Williamson-Hall

https://doi.org/10.1021/jacs.5c08223
J. Am. Chem. Soc. XXXX, XXX, XXX−XXX

analysis provides direct validation of these structural modifications. Furthermore, DFT calculations reveal that strain-induced lattice distortions annihilate the Weyl points in the nanosheets, opening a band gap and stabilizing the semiconducting state. Charge transport in these nanosheets follows Mott's variable-range hopping mechanism, while temperature-dependent conductivity measurements suggest a coexistence of semiconducting and weakly gapless electronic features. Magnetic characterization confirms the retention of robust ferromagnetism, with a Curie temperature of ∼100 K. These findings highlight the crucial role of dimensionality and strain engineering in tailoring the electronic properties of magnetic Weyl semimetals, paving the way for their potential applications in spintronic and quantum technologies.

■ ASSOCIATED CONTENT

Supporting Information

The Supporting Information is available free of charge at https://pubs.acs.org/doi/10.1021/jacs.5c08223.

Experimental section, PXRD, additional FESEM images, magnetic moment, hopping mechanism, electronic structure for bulk and monolayer with different tensile strain, W−H plot, Tables S1−S15 (PDF)

■ AUTHOR INFORMATION

Corresponding Author

Subhajit Roychowdhury − *Department of Chemistry, Indian Institute of Science Education and Research Bhopal, Bhopal 462 066, India;* orcid.org/0000-0002-1808-9432; Email: subhajit@iiserb.ac.in

Authors

Abhinav Pancholi − *Department of Chemistry, Indian Institute of Science Education and Research Bhopal, Bhopal 462 066, India*

Pranav Negi − *Department of Chemistry, Indian Institute of Science Education and Research Bhopal, Bhopal 462 066, India*

Kartik Samanta − *Department of Physics and Astronomy & Nebraska Center for Materials and Nanoscience, University of Nebraska, Lincoln, Nebraska 68588, United States; Department of Physics and Materials Science and Engineering, Jaypee Institute of Information Technology, Noida 201304, India*

Abhishek Das − *Department of Chemistry, Indian Institute of Science Education and Research Bhopal, Bhopal 462 066, India*

Premakumar Yanda − *Max Planck Institute for Chemical Physics of Solids, Dresden 01187, Germany;* orcid.org/0000-0001-9798-1236

Shishir Kumar Pandey − *Department of General Science, Birla Institute of Technology and Science, Pilani, Dubai 345055, UAE;* orcid.org/0000-0003-0204-5205

Complete contact information is available at: https://pubs.acs.org/10.1021/jacs.5c08223

Author Contributions

#A.P. and P.N. contributed equally to this work.

Notes

The authors declare no competing financial interest.

■ ACKNOWLEDGMENTS

P.N. thanks the IISER Bhopal for a fellowship. S.R. acknowledges CIF facilities of IISER Bhopal for characterizations and measurements and financial support from PM Early Career Research Grant (ANRF/ECRG/2024/001151/CS), Anusandhan National Research Foundation (ANRF) and IISER Bhopal.

■ REFERENCES

(1) Kumar, N.; Guin, S. N.; Manna, K.; Shekhar, C.; Felser, C. Topological Quantum Materials from the Viewpoint of Chemistry. *Chem. Rev.* **2021**, *121* (5), 2780−2815.

(2) Schoop, L. M.; Pielnhofer, F.; Lotsch, B. V. Chemical Principles of Topological Semimetals. *Chem. Mater.* **2018**, *30* (10), 3155−3176.

(3) Tokura, Y.; Yasuda, K.; Tsukazaki, A. Magnetic Topological Insulators. *Nat. Rev. Phys.* **2019**, *1* (2), 126−143.

(4) Bernevig, B. A.; Felser, C.; Beidenkopf, H. Progress and Prospects in Magnetic Topological Materials. *Nature* **2022**, *603* (7899), 41−51.

(5) Moore, J. E. The Birth of Topological Insulators. *Nature* **2010**, *464* (7286), 194−198.

(6) Novoselov, K. S.; Geim, A. K.; Morozov, S. V.; Jiang, D.; Zhang, Y.; Dubonos, S. V.; Grigorieva, I. V.; Firsov, A. A. Electric Field Effect in Atomically Thin Carbon Films. *Science* **2004**, *306* (5696), 666−669.

(7) Duong, D. L.; Yun, S. J.; Lee, Y. H. Van Der Waals Layered Materials: Opportunities and Challenges. *ACS Nano* **2017**, *11* (12), 11803−11830.

(8) Novoselov, K. S.; Fal'ko, V. I.; Colombo, L.; Gellert, P. R.; Schwab, M. G.; Kim, K. A Roadmap for Graphene. *Nature* **2012**, *490* (7419), 192−200.

(9) Novoselov, K. S.; Mishchenko, A.; Carvalho, A.; Castro Neto, A. H. 2D Materials and van Der Waals Heterostructures. *Science* **2016**, *353* (6298), No. aac9439.

(10) Huang, B.; Clark, G.; Navarro-Moratalla, E.; Klein, D. R.; Cheng, R.; Seyler, K. L.; Zhong, D.; Schmidgall, E.; McGuire, M. A.; Cobden, D. H.; Yao, W.; Xiao, D.; Jarillo-Herrero, P.; Xu, X. Layer-Dependent Ferromagnetism in a van Der Waals Crystal down to the Monolayer Limit. *Nature* **2017**, *546* (7657), 270−273.

(11) Gong, C.; Li, L.; Li, Z.; Ji, H.; Stern, A.; Xia, Y.; Cao, T.; Bao, W.; Wang, C.; Wang, Y.; Qiu, Z. Q.; Cava, R. J.; Louie, S. G.; Xia, J.; Zhang, X. Discovery of Intrinsic Ferromagnetism in Two-Dimensional van Der Waals Crystals. *Nature* **2017**, *546* (7657), 265−269.

(12) Deng, Y.; Yu, Y.; Song, Y.; Zhang, J.; Wang, N. Z.; Sun, Z.; Yi, Y.; Wu, Y. Z.; Wu, S.; Zhu, J.; Wang, J.; Chen, X. H.; Zhang, Y. Gate-Tunable Room-Temperature Ferromagnetism in Two-Dimensional Fe_3GeTe_2. *Nature* **2018**, *563* (7729), 94−99.

(13) Li, B.; Wan, Z.; Wang, C.; Chen, P.; Huang, B.; Cheng, X.; Qian, Q.; Li, J.; Zhang, Z.; Sun, G.; Zhao, B.; Ma, H.; Wu, R.; Wei, Z.; Liu, Y.; Liao, L.; Ye, Y.; Huang, Y.; Xu, X.; Duan, X.; Ji, W.; Duan, X. Van Der Waals Epitaxial Growth of Air-Stable $CrSe_2$ Nanosheets with Thickness-Tunable Magnetic Order. *Nat. Mater.* **2021**, *20* (6), 818−825.

(14) Li, Y.; Zhou, Z.; Shen, P.; Chen, Z. Spin Gapless Semiconductor−Metal−Half-Metal Properties in Nitrogen-Doped Zigzag Graphene Nanoribbons. *ACS Nano* **2009**, *3* (7), 1952−1958.

(15) Wang, X. L. Proposal for a New Class of Materials: Spin Gapless Semiconductors. *Phys. Rev. Lett.* **2008**, *100* (15), No. 156404.

(16) Ouardi, S.; Fecher, G. H.; Felser, C.; Kübler, J. Realization of Spin Gapless Semiconductors: The Heusler Compound Mn_2CoAl. *Phys. Rev. Lett.* **2013**, *110* (10), No. 100401.

(17) Wang, J.; Wang, D. Two-Dimensional Spin-Gapless Semiconductors: A Mini-Review. *Front. Chem.* **2022**, *10*, No. 996344.

(18) Mishra, V.; Kumar, A.; Pandey, L.; Gupta, N. K.; Hait, S.; Barwal, V.; Sharma, N.; Kumar, N.; Chandra, S.; Chaudhary, S. Disordered Spin Gapless Semiconducting CoFeCrGa Heusler Alloy Thin Films on Si (100): Experiment and Theory. *Nanoscale* **2022**, *15* (1), 337−349.

(19) Kharel, P.; Zhang, W.; Skomski, R.; Valloppilly, S.; Huh, Y.; Fuglsby, R.; Gilbert, S.; Sellmyer, D. J. Magnetism, Electron Transport and Effect of Disorder in CoFeCrAl. *J. Phys. D: Appl. Phys.* **2015**, *48* (24), No. 245002.
(20) Stephen, G. M.; Lane, C.; Buda, G.; Graf, D.; Kaprzyk, S.; Barbiellini, B.; Bansil, A.; Heiman, D. Electrical and Magnetic Properties of Thin Films of the Spin-Filter Material CrVTiAl. *Phys. Rev. B* **2019**, *99* (22), No. 224207.
(21) Liu, E.; Sun, Y.; Kumar, N.; Muechler, L.; Sun, A.; Jiao, L.; Yang, S.-Y.; Liu, D.; Liang, A.; Xu, Q.; Kroder, J.; Süß, V.; Borrmann, H.; Shekhar, C.; Wang, Z.; Xi, C.; Wang, W.; Schnelle, W.; Wirth, S.; Chen, Y.; Goennenwein, S. T. B.; Felser, C. Giant Anomalous Hall Effect in a Ferromagnetic Kagome-Lattice Semimetal. *Nat. Phys.* **2018**, *14* (11), 1125−1131.
(22) Liu, D. F.; Liang, A. J.; Liu, E. K.; Xu, Q. N.; Li, Y. W.; Chen, C.; Pei, D.; Shi, W. J.; Mo, S. K.; Dudin, P.; Kim, T.; Cacho, C.; Li, G.; Sun, Y.; Yang, L. X.; Liu, Z. K.; Parkin, S. S. P.; Felser, C.; Chen, Y. L. Magnetic Weyl Semimetal Phase in a Kagomé Crystal. *Science* **2019**, *365* (6459), 1282−1285.
(23) Weihrich, R.; Anusca, I.; Zabel, M. Halbantiperowskite: Zur Struktur der Shandite $M_{3/2}AS$ (M = Co, Ni; A = In, Sn) und ihren Typ-Antitypbeziehungen. *Z. Anorg. Allg. Chem.* **2005**, *631* (8), 1463−1470.
(24) Geishendorf, K.; Schlitz, R.; Vir, P.; Shekhar, C.; Felser, C.; Nielsch, K.; Goennenwein, S. T. B.; Thomas, A. Magnetoresistance and Anomalous Hall Effect in Micro-Ribbons of the Magnetic Weyl Semimetal $Co_3Sn_2S_2$. *Appl. Phys. Lett.* **2019**, *114* (9), No. 092403.
(25) Li, S.; Gu, G.; Liu, E.; Cheng, P.; Feng, B.; Li, Y.; Chen, L.; Wu, K. Epitaxial Growth and Transport Properties of Magnetic Weyl Semimetal $Co_3Sn_2S_2$ Thin Films. *ACS Appl. Electron. Mater.* **2020**, *2* (1), 126−133.
(26) Chen, G.; Long, B.; Jin, L.; Zhang, H.; Cheng, Z.; Zhang, X.; Liu, G. Synthesis of Weyl Semi-Metal $Co_3Sn_2S_2$ by Hydrothermal Method and Its Physical Properties. *Metals* **2022**, *12* (5), No. 830.
(27) Huang, B.; Clark, G.; Navarro-Moratalla, E.; Klein, D. R.; Cheng, R.; Seyler, K. L.; Zhong, D.; Schmidgall, E.; McGuire, M. A.; Cobden, D. H.; Yao, W.; Xiao, D.; Jarillo-Herrero, P.; Xu, X. Layer-Dependent Ferromagnetism in a van Der Waals Crystal down to the Monolayer Limit. *Nature* **2017**, *546* (7657), 270−273.
(28) Gong, C.; Li, L.; Li, Z.; Ji, H.; Stern, A.; Xia, Y.; Cao, T.; Bao, W.; Wang, C.; Wang, Y.; Qiu, Z. Q.; Cava, R. J.; Louie, S. G.; Xia, J.; Zhang, X. Discovery of Intrinsic Ferromagnetism in Two-Dimensional van Der Waals Crystals. *Nature* **2017**, *546* (7657), 265−269.
(29) Deng, Y.; Yu, Y.; Song, Y.; Zhang, J.; Wang, N. Z.; Sun, Z.; Yi, Y.; Wu, Y. Z.; Wu, S.; Zhu, J.; Wang, J.; Chen, X. H.; Zhang, Y. Gate-Tunable Room-Temperature Ferromagnetism in Two-Dimensional Fe_3GeTe_2. *Nature* **2018**, *563* (7729), 94−99.
(30) Li, B.; Wan, Z.; Wang, C.; Chen, P.; Huang, B.; Cheng, X.; Qian, Q.; Li, J.; Zhang, Z.; Sun, G.; Zhao, B.; Ma, H.; Wu, R.; Wei, Z.; Liu, Y.; Liao, L.; Ye, Y.; Huang, Y.; Xu, X.; Duan, X.; Ji, W.; Duan, X. Van Der Waals Epitaxial Growth of Air-Stable $CrSe_2$ Nanosheets with Thickness-Tunable Magnetic Order. *Nat. Mater.* **2021**, *20* (6), 818−825.
(31) Mishra, V.; Barwal, V.; Pandey, L.; Kumar Gupta, N.; Hait, S.; Kumar, A.; Sharma, N.; Kumar, N.; Chaudhary, S. Investigation of Spin Gapless Semiconducting Behaviour in Quaternary CoFeMnSi Heusler Alloy Thin Films on Si (100). *J. Magn. Magn. Mater.* **2022**, *547*, No. 168837.
(32) Bainsla, L.; Mallick, A. I.; Raja, M. M.; Coelho, A. A.; Nigam, A. K.; Johnson, D. D.; Alam, A.; Suresh, K. G. Origin of Spin Gapless Semiconductor Behavior in CoFeCrGa: Theory and Experiment. *Phys. Rev. B* **2015**, *92* (4), No. 045201.
(33) Buckley, R. G.; Butler, T.; Pot, C.; Strickland, N. M.; Granville, S. Exploring Disorder in the Spin Gapless Semiconductor Mn_2CoAl. *Mater. Res. Express* **2019**, *6* (10), No. 106113.
(34) Winkler, M. T.; Recht, D.; Sher, M.-J.; Said, A. J.; Mazur, E.; Aziz, M. J. Insulator-to-Metal Transition in Sulfur-Doped Silicon. *Phys. Rev. Lett.* **2011**, *106* (17), No. 178701.
(35) Shklovskii, B. I.; Efros, A. L. *Electronic Properties of Doped Semiconductors*; Springer Berlin Heidelberg: Berlin, Heidelberg, 1984; Vol. *45*.
(36) Zhang, J.; Jin, L.; Chen, J.; Zhang, C.; Li, P.; Yuan, Y.; Wen, Y.; Zhang, Q.; Zhang, X.; Liu, E.; Wang, W.; Zhang, X. Modulation of Weyl Semimetal State in Half-Heusler GdPtBi Enabled by Hydrostatic Pressure. *New J. Phys.* **2021**, *23* (8), No. 083041.
(37) Rodríguez, M.; Bonalde, I.; Medina, E. Consistent Hopping Criterion in the Efros-Shklovskii Regime. *Phys. Rev. B* **2007**, *75* (23), No. 235205.
(38) Guin, S. N.; Vir, P.; Zhang, Y.; Kumar, N.; Watzman, S. J.; Fu, C.; Liu, E.; Manna, K.; Schnelle, W.; Gooth, J.; Shekhar, C.; Sun, Y.; Felser, C. Zero-Field Nernst Effect in a Ferromagnetic Kagome-Lattice Weyl-Semimetal $Co_3Sn_2S_2$. *Adv. Mater.* **2019**, *31* (25), No. 201806622.
(39) Rathod, S.; Megha; Lakhani, A.; Kumar, D. Effect of Crystalline Quality on the Transport Properties of Ferromagnetic Weyl Semimetal $Co_3Sn_2S_2$. *J. Solid State Chem.* **2020**, *289*, No. 121461.



https://doi.org/10.1021/jacs.5c08223
J. Am. Chem. Soc. XXXX, XXX, XXX−XXX